ChemComm

COMMUNICATION

View Article Online
View Journal | View Issue

Check for updates

Cite this: *Chem. Commun.*, 2025, 61, 2758

Received 17th December 2024,
Accepted 13th January 2025

DOI: 10.1039/d4cc06599a

rsc.li/chemcomm

Published on 13 January 2025. Downloaded on 2026-05-12 3:05:32 PM.

Enhancing open-circuit voltage in $FAPbI_3$ perovskite solar cells *via* self-formation of coherent buried interface $FAPbI_xCl_{3-x}$†

Cuina Gao,[a] Sihui Jia,[a] Xiaofei Yin,[b] Zhi Li,[b] Guang Yang,[a] Jing Chen, *[a] Zhaoqian Li *[c] and Xingtao An *[a]

The interfaces between the perovskite and charge-transporting layers typically exhibit high defect concentrations, which are the primary cause of open-circuit voltage loss. Passivating the interface between the perovskite and electron-transporting layer is particularly challenging due to the dissolution of surface treatment agents during the perovskite coating. In this study, a coherent $FAPbI_xCl_{3-x}$ buried interface was simultaneously formed during the preparation of $FAPbI_3$. This interlayer significantly improved charge extraction and transportation from the perovskite layer, while reducing trap state density. As a result, the open-circuit voltage increased from 1.01 V to 1.10 V, with the PCE improved from 19.05% to 22.89%.

Although the photovoltaic conversion efficiency (PCE) of perovskite solar cells (PSCs) continues to improve with the current highest PCE exceeding 26%,[1] there remains a gap to the theoretical Shockley–Queisser limit (S–Q limit). For photovoltaic devices, short-circuit current density (J_{SC}), open-circuit voltage (V_{OC}), and fill factor (FF) are crucial parameters that determine the performance of PSCs. Significant breakthroughs have been achieved in J_{SC} and FF in the research progress of PSCs. The enhancement of V_{OC} is a key factor in improving the PCE of PSCs.[2–4] The non-radiative recombination process during charge transportation is the main obstacle to the loss of V_{OC}. The non-radiative recombination primarily occurs at the perovskite grain boundaries, on the surface, and within the perovskite film. It has been reported that the interfaces between the perovskite and charge-transporting layers often contain high concentrations of defects, particularly deep-level defects, which significantly reduce the PCE of PSCs.[5–7] Non-radiative recombination at the interface between the perovskite and charge-transporting layers accelerates the degradation of the perovskite layer, thereby hindering its practical application.[8–10] In addition to enhancing the quality of the perovskite film, establishing an effective interface between the perovskite and charge transport layers is essential for minimizing non-radiative recombination. The characterization and optimization of the passivization layer at the perovskite/hole transport layer (HTL) interface are relatively straightforward.[11–13] Various research groups have effectively reduced interface defects by employing strategies such as using polymers,[14–16] alkyl halide ammoniums,[17–19] organic ammonium salts,[20] and so on. Excellent progress has been made in reducing V_{OC} loss and enhancing device performance and stability. However, the surface treatment agents on the electron transport layer (ETL) may dissolve during the perovskite coating process, which would degrade the interface passivization layer potentially. This can result in sub-optimal interface modification and the formation of additional interface defects.[21]

In this work, a coherent interface $FAPbI_xCl_{3-x}$ was simultaneously formed during the preparation of $FAPbI_3$ *via* a vapor–solid reaction. This approach eliminated the dissolution phenomenon typically observed during the spin-coating of the perovskite precursor solution.[22–25] The resulting interface exhibited excellent lattice matching with the perovskite layer, which facilitated effective electron transport, reduced interface defects, and enhanced the V_{OC} of the PSCs from 1.01 V to 1.10 V.

The target samples were prepared by incorporating $PbCl_2$ at a concentration of 10%, as detailed in the Experimental section of the ESI.† Perovskite films and devices without $PbCl_2$ incorporation were designated as the control samples. The surface morphology of the perovskite films was analyzed using scanning electron microscopy (SEM). As shown in Fig. 1a, both the control and target perovskite films exhibit uniform morphology and similar compact textures, with no observable pinholes. The target perovskite film shows a larger average grain size

[a] College of Science, Hebei University of Science and Technology, 26 Yuxiang Road, Shijiazhuang 050018, P. R. China
[b] Changzhou Houde Renewable Resources Technology Company Limited, Jiangsu, Changzhou 213133, P. R. China
[c] Institute of Solid State Physics, Hefei Institutes of Physical Science, Chinese Academy of Sciences, Hefei, Anhui 230031, P. R. China

† Electronic supplementary information (ESI) available. See DOI: https://doi.org/10.1039/d4cc06599a

This journal is © The Royal Society of Chemistry 2025

Published on 13 January 2025. Downloaded on 2026-05-12 3:05:32 PM.

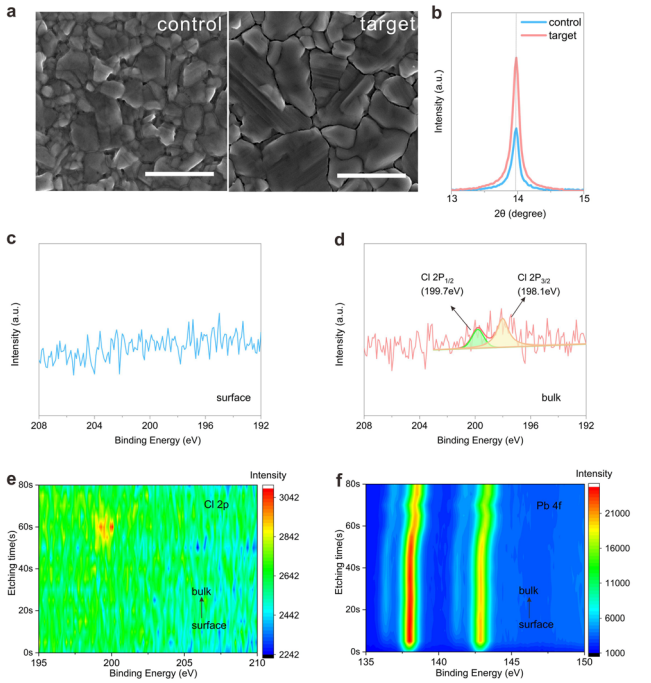

Fig. 1 (a) Top-view SEM images of control and target perovskite films; scale bars: 2 μm. (b) XRD patterns of the control and target perovskite films with the angle enlarged at 13.9°. XPS spectra of the distribution of Cl elements on the surface (c) and bulk (d) within the target film. The contour maps of XPS depth profile for the Cl 2p peaks (e) and Pb 4d peaks (f) of the target perovskite films. Gradient colors represent intensity.

compared to the control, which reduces grain boundaries and defects. To determine the location of the Cl element, we first performed XRD (Fig. S1, ESI†) and XPS analyses on the control and target perovskite films for comparison. The enlarged view of the XRD patterns for all the samples at 13.9° is shown in Fig. 1b. No shifting of the peak position was observed, meaning that the surface of the final films is $FAPbI_3$. At the same time, the XPS analysis did not detect any Cl element on the surface of the target film either (Fig. 1c). However, the intensity of the Cl peaks at 199.7 eV for Cl $2p_{1/2}$ and 198.1 eV for Cl $2p_{3/2}$ is shown in the bulk of the target film (Fig. 1d). To further confirm the presence of Cl within the bulk of the perovskite film, XPS measurements were conducted at different depths on the prepared target $FAPbI_3$ (Fig. 1e and f). Throughout the etching process from 0 s to 50 s, no Cl signal was detected in $FAPbI_3$, and the Pb peak remained unchanged. This suggests that the perovskite film within the etching depth from 0 s to 50 s is composed of $FAPbI_3$. After 50 s of etching time, the Cl signal began to appear. As shown in Fig. S2 (ESI†), the Cl distribution in the bulk of the target film was observed at etching times from 45 s to 70 s. It can be observed that the Cl signal is detected starting at 50 s and disappears at 65 s. As the etching time increases, the Cl 2p peak shifts towards a higher binding energy. The Pb 4f peaks shifted gradually towards higher binding energy starting at 50 s. The peak shifting of Pb and Cl was ascribed to the introduction of Cl into the $FAPI_3$ lattice, which resulted in the improvement of chemical bonding.[23] At an etching time of 65 s, the Sn signal appeared (Fig. S3, ESI†), while the Pb and Cl signals began to disappear. The XRD results of the vapor–solid reaction at 3 min, 8 min, 15 min and 30 min (target film) are shown in Fig. S4 (ESI†). As the reaction proceeds, the perovskite characteristic peaks gradually shift toward 14° of controlled $FAPbI_3$. The shift of the characteristic peaks indicates that substitution has occurred between I and Cl. This suggests the formation of an $FAPbI_xCl_{3-x}$ layer between SnO_2 and $FAPbI_3$. With increasing etching time, the peaks of Pb 4f and Cl 2p shifted towards higher energy gradually. It was indicated that as the film depth increases, the content of Cl gradually increases. This leads to the formation of a gradient distribution of $FAPbI_xCl_{3-x}$.

The vapor–solid reaction was employed to prepare $FAPbI_3$. In the reaction process the coherent interface layer $FAPbI_xCl_{3-x}$ was generated simultaneously. As shown in Fig. S5 (ESI†), the characteristic peaks of $PbI_2/PbCl_2$ remained consistent with PbI_2. The 12.65° of $PbI_2/PbCl_2$ exhibited a shift compared to 12.6° of pure PbI_2. This indicates that the $PbI_2/PbCl_2$ forms a pure compound, which was labelled as PbI_xCl_{2-x} in the subsequent discussion. Fig. 2a depicts the schematic diagram of the perovskite film preparation process. The PbI_xCl_{2-x} was spin-coated onto the SnO_2 substrate. After annealing at 70 °C, the PbI_xCl_{2-x} film was placed in an FAI vapor environment at 170 °C for reaction. The target perovskite films $FAPbI_3$/$FAPbI_xCl_{3-x}$ can be obtained through a single-step vapor–solid reaction. Fig. 2b illustrates the possible evolution of the nucleation and crystallization processes of $FAPbI_3$ perovskite films with or without $PbCl_2$. PbI_2 and $PbCl_2$ are mixed in a certain ratio to form PbI_xCl_{2-x}. During the reaction of PbI_xCl_{2-x} film with FAI vapor, the $FAPbI_xCl_{3-x}$ was formed. With the vapor–solid reaction proceeding, due to the Cl having much weaker bond affinity to Pb than I in the lattice under the 170 °C reaction temperature, the I ion and Cl ion exchanged gradually and the Cl ion sublimates in the form of FACl.[23] By controlling the reaction time to 20 minutes, the $FAPbI_xCl_{3-x}$ in the buried layer had not yet undergone complete substitution. The $FAPbI_3$/$FAPbI_xCl_{3-x}$ film was obtained simultaneously through a single

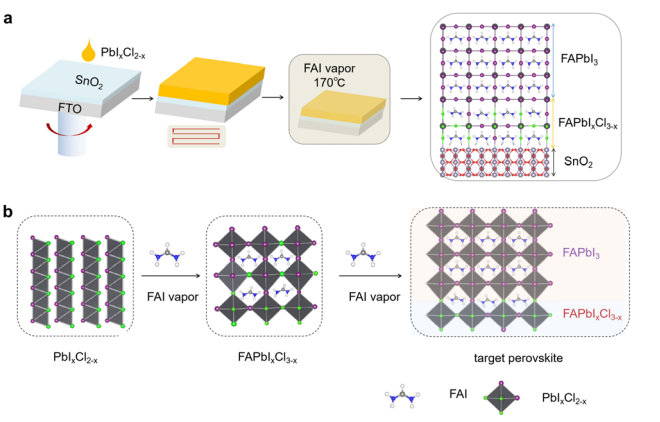

Fig. 2 Schematic diagram of (a) perovskite films prepared with or without $PbCl_2$ and (b) the possible phase evolution of the nucleation and crystallization of the target $FAPbI_3$.

Published on 13 January 2025. Downloaded on 2026-05-12 3:05:32 PM.

vapor–solid reaction process. Not only was the dissolution issue that often arises when spin-coating the perovskite precursor eliminated, but also the buried layer of $FAPbI_xCl_{3-x}$ and $FAPbI_3$ exhibits perfect lattice matching. It is important to note that further research is needed to better understand the specific reaction time and the corresponding thickness of the $FAPbI_xCl_{3-x}$ layer.

It has been reported that interface Cl atoms enhance the binding energy at the perovskite/ETL interface and promote strong electron coupling. Due to the high formation energy of Pb–Cl anti-sites, the formation of deep-level defects is suppressed, resulting in a lower density of interface trap states.[26] The optical properties of both the control and target perovskite films were further explored by using ultraviolet-visible (UV-Vis) absorption and photoluminescence (PL) spectra. As shown in Fig. 3a, the absorption edges of both perovskite films are all ~810 nm, showing excellent absorption ability. Compared to the control film, the target film exhibited a higher light absorption. This improved absorbance stems from the presence of the buried layer $FAPbI_xCl_{3-x}$. The $FAPbI_xCl_{3-x}$ improved the film quality with increased grain size and crystallization, which would suppress the non-radiative recombination caused. It was indicated that the buried interface promoted the extraction and transportation of the carriers.[27] The steady-state PL intensity of the target film is an order of magnitude higher than that of the control film, indicating that the formation of $FAPbI_xCl_{3-x}$ could effectively reduce the trap density, thus minimizing the non-radiative recombination in perovskite films. Time-resolved photoluminescence (TRPL) measurements were conducted to study the carrier transport and recombination in the perovskite layer. As shown in Fig. 3b, the recombination in TRPL was dominated by second-order trap-assisted recombination. The fitted lifetime of the target film is five times longer than that of the control film (Table S1, ESI†). This substantial increase in carrier lifetime suggests a lower non-radiative recombination, which is attributed to the reduced density of trap states in the target film. Therefore, space-charge-limited current (SCLC) measurement was employed to investigate the trap density (N_{trap}) of perovskite films (Fig. 3c). The dark *J–V* curves were measured from an electron-injecting device. Fig. 3c describes the dark *J–V* curves of devices based on the control and target film, respectively. The voltage (V_{TFL}) which marked the transition from the ohmic region to the trap-filled limit (TFL) region is used to calculate the trap state density by eqn (S1) (ESI†). From the *J–V* curves, it can be seen that the V_{TFL} of the control device and target devices is 0.735 V and 0.627 V, respectively. The corresponding trap state density decreased from 5.76×10^{15} cm^{-3} of the control film to 4.92×10^{15} cm^{-3} of the target film, which was consistent with the results of TRPL measurement. The low trap state density of perovskite film might associate with the enhanced V_{OC} of the corresponding devices. The intrinsic mobility distribution, estimated by SCLC, is shown in Fig. 3c. It increased from 0.179 cm^2 V^{-1} s^{-1} for the control film to 0.243 cm^2 V^{-1} s^{-1} for the target film. The V_{OC} decay is one of the effective methods to analyze the electron recombination process in the anode and perovskite film. Fig. 3d shows the V_{OC} decay curves of PSCs based on the control film and target film, respectively. Three electron transport processes in different voltage regions explained the decay curves effectively. The exponential increase in the voltage region reflects internal trapping and de-trapping of electrons in bulk perovskite materials, which is the critical consideration of the obtained $FAPbI_3$ layer with a different reaction process. The electron lifetime can be calculated through eqn (S2) (ESI†). The PSCs based on the target had a much longer τ_n than that of the control. For example, at the voltage of 0.3 V, the τ_n are 0.27 s and 1.22 s of PSCs based on the control and target, respectively. The $FAPbI_xCl_{3-x}$ would increase the electron lifetime and reduce the charge recombination rate in the perovskite layer.

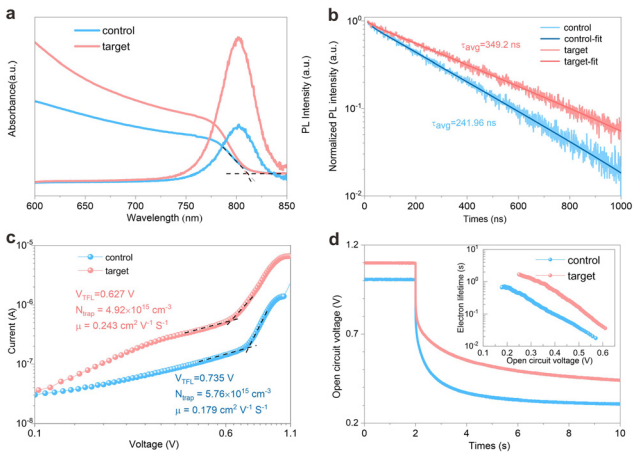

Fig. 3 (a) UV-vis absorption spectra and steady-state PL spectra of control and target perovskite films excited from the perovskite side. (b) Time-resolved photoluminescence (TRPL) spectra for control and target perovskite films. (c) SCLC measurement for electron-only devices with a device configuration of FTO/SnO_2/perovskite/Au. (d) Transient photovoltage decay curves and the relationship between extracted lifetime of the injected carriers in the devices and V_{oc} of the PSCs based on the control and target.

As expected from the defect concentration and carrier lifetime analysis of the perovskite films formed under each condition, the average power conversion efficiency (PCE_{avg}) of the target devices was significantly higher than that of the control devices. The PCE_{avg} of the target and control was 22.22% and 18.61%, respectively. The overall improvement in the target devices is primarily attributed to the enhancement of the V_{OC} and FF. The champion device offers a high PCE of 22.89% for the reverse scan (J_{SC} of 24.89 mA cm^{-2}, a V_{OC} of 1.10 V, and an FF of 79.8%) and a PCE of 22.03% for the forward scan (J_{SC} of 24.77 mA cm^{-2}, a V_{OC} of 1.09 V and an FF of 77.6%), showing a negligible hysteresis of 3.1% compared with the control device of 19.05% for the reverse scan and 17.65% for the forward scan, as shown in Fig. 4a and Table S2 (ESI†). The incident photon-to-current efficiencies (IPCEs) of both the control and target devices were measured, and the integrated currents correspond well with the J_{SC} values obtained from the *J–V* curves (Fig. 4b). A stabilized PCE of 22.89% for the target PSC is achieved after 200 seconds of continuous maximum

 This journal is © The Royal Society of Chemistry 2025

Published on 13 January 2025. Downloaded on 2026-05-12 3:05:32 PM.

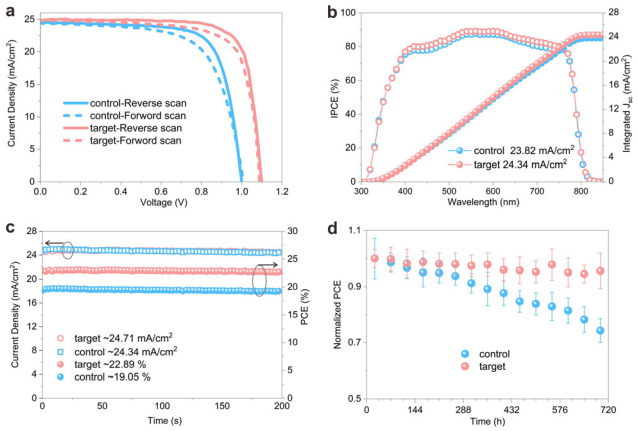

Fig. 4 (a) *J*–*V* curves measured in reverse and forward scan modes for the champion control and target PSCs. (b) IPCE (left axis) and corresponding integrated J_{SC} (right axis) for the control and target PSCs. (c) Stabilized efficiency after maximum power point tracking (MPPT) of the control and target devices for 200 s. (d) Normalized PCE of devices based on the control and target films in 30 days under continuous one-sun illumination in a N_2 environment at a room temperature of 25 °C.

power point tracking (MPPT), as shown in Fig. 4c, while the control device shows a considerably lower stabilized output of 19.05%. As shown in Fig. 4d, the unencapsulated target PSC retained 90.0% of its initial efficiency after 30 days under continuous one-sun illumination in the N_2 environment. In contrast, the control device degraded to 74.0% of its initial efficiency.

In summary, this study presents a vapor–solid reaction method for preparing $FAPbI_3$ perovskite, which simultaneously forms a coherent interface $FAPbI_xCl_{3-x}$ passivization layer at the buried interface. The $FAPbI_xCl_{3-x}$ shows excellent lattice matching with $FAPbI_3$, effectively reducing interface charge recombination and enhancing charge transport. Furthermore, the chlorine atoms at the $FAPbI_xCl_{3-x}$ film strengthen the binding energy between the perovskite and the ETL, suppressing anti-site defects and lowering the density of interface trap states. This method also avoids the dissolution of the passivization layer at the buried interface during perovskite spin-coating. In conclusion, the $FAPbI_3$ films with the coherent interface layer $FAPbI_xCl_{3-x}$ are simultaneously prepared using a single-step vapor–solid reaction. As a result, the V_{OC} was increased from 1.01 V to 1.10 V, with the PCE improved from 19.05% to 22.89%.

This work was supported by the Natural Science Foundation of Hebei Province (F2023208017 and A2021208015).

Data availability

The authors confirm that the data supporting the findings of this study are available within the article.

Conflicts of interest

There are no conflicts to declare.

Notes and references

1 https://www.nrel.gov/pv/cell-efficiency.html.
2 Y. Zhang, R. Yu, M. Li, Z. He, Y. Dong, Z. Xu, R. Wang, Z. Ma and Z. Tan, *Adv. Mater.*, 2024, **36**, e2310203.
3 K. Wang, L. Zheng, Y. Hou, A. Nozariasbmarz, B. Poudel, J. Yoon, T. Ye, D. Yang, A. V. Pogrebnyakov and V. Gopalan, *Joule*, 2022, **6**, 756–771.
4 C. Luo, G. Zheng, F. Gao, X. Wang, C. Zhan, X. Gao and Q. Zhao, *Nat. Photonics*, 2023, **17**, 856–864.
5 G. Liu, X. Jiang, W. Feng, G. Yang, X. Chen, Z. Ning and W. Q. Wu, *Angew. Chem., Int. Ed.*, 2023, **62**, e202305551.
6 C. Wang, J. Wu, S. Wang, Z. Yan, X. Liu, G. Li, L. Chen, S. Zhu, W. Sun and Z. Lan, *Solar RRL*, 2022, **6**, 2100995.
7 C. Zhao, Q. Zhang, Y. Lyu, J. Liu, F. Shen, H. Liu, H. Kong, H. Han, A. Krishna and J. Xu, *Adv. Funct. Mater.*, 2024, **34**, 2404099.
8 H. Han, J. Xu, H. Liu, Y. Fu, C. Zhao, R. Shi, H. Zhang and J. Yao, *ACS Energy Lett.*, 2023, **8**, 4608–4616.
9 Z. Li, Y. Ren, W. Chen, T. Wei, L. Mo, Y. Huang, H. Zhang, G. Cao and L. Hu, *Renewables*, 2023, **1**, 572–581.
10 L. Zhang, L. Mei, K. Wang, Y. Lv, S. Zhang, Y. Lian, X. Liu, Z. Ma, G. Xiao and Q. Liu, *Nano-Micro Lett.*, 2023, **15**, 177.
11 F. Cao, Z. Zhu, C. Zhang, P. Chen, S. Wang, A. Tong, R. He, Y. Wang, W. Sun and Y. Li, *Small*, 2023, **19**, 2207784.
12 C. Zhao, H. Zhang, A. Krishna, J. Xu and J. Yao, *Adv. Opt. Mater.*, 2024, **12**, 2301949.
13 C. Zhao, H. Zhang, M. Almalki, J. Xu, A. Krishna, F. T. Eickemeyer, J. Gao, Y. M. Wu, S. M. Zakeeruddin and J. Chu, *Adv. Mater.*, 2023, **35**, 2211619.
14 H. Li, C. Zhang, C. Gong, D. Zhang, H. Zhang, Q. Zhuang, X. Yu, S. Gong, X. Chen, J. Yang, X. Li, R. Li, J. Li, J. Zhou, H. Yang, Q. Lin, J. Chu, M. Grätzel, J. Chen and Z. Zang, *Nat. Energy*, 2023, **8**, 946–955.
15 S. Zhang, F. Ye, X. Wang, R. Chen, H. Zhang, L. Zhan, X. Jiang, Y. Li, X. Ji and S. Liu, *Science*, 2023, **380**, 404–409.
16 C. Liu, Y. Yang, H. Chen, J. Xu, A. Liu, A. S. Bati, H. Zhu, L. Grater, S. S. Hadke and C. Huang, *Science*, 2023, **382**, 810–815.
17 J. Zhang, B. Yu, Y. Sun and H. Yu, *Adv. Energy Mater.*, 2023, **13**, 2300382.
18 Y. Zhou, Z. Wang, J. Jin, X. Zhang, J. Zou, F. Yao, Z. Zhu, X. Cui, D. Zhang and Y. Yu, *Angew. Chem., Int. Ed.*, 2023, **62**, e202300759.
19 Y. W. Jang, S. Lee, K. M. Yeom, K. Jeong, K. Choi, M. Choi and J. H. Noh, *Nat. Energy*, 2021, **6**, 63–71.
20 Q. Chen, J. Wu, X. Liu, Y. Du, C. Deng, X. Chen, L. Sun, L. Tan, W. Sun and Z. Lan, *ACS Appl. Mater. Interfaces*, 2024, **16**, 8949–8959.
21 H. Min, D. Y. Lee, J. Kim, G. Kim, K. S. Lee, J. Kim, M. J. Paik, Y. K. Kim, K. S. Kim and M. G. Kim, *Nature*, 2021, **598**, 444–450.
22 C. Duan, J. Zhong, S. Hu, Y. Dou, J. Lu, Y. B. Cheng and Z. Ku, *Adv. Funct. Mater.*, 2024, **34**, 2313435.
23 J. Chen, J. Xu, C. Zhao, B. Zhang, X. Liu, S. Dai and J. Yao, *ACS Appl. Mater. Interfaces*, 2019, **11**, 4597–4606.
24 Y. Ren, H. Fu, Y. Li, Z. Li, C. Li and X. An, *Chem. Commun.*, 2024, **60**, 2938–2941.
25 Y. Ren, J. Chen, D. Ji, Y. Sun and C. Li, *Chem. Eng. J.*, 2020, **384**, 123273.
26 E. Mosconi, E. Ronca and F. De Angelis, *J. Phys. Chem. Lett.*, 2014, **5**, 2619–2625.
27 C. Ge, L. Xie, J. Yang, K. Wei, T. Wu, L. Wang, L. Sun, J. Zhang and Y. Hua, *Adv. Funct. Mater.*, 2024, **34**, 2313688.